International Journal of Research in Engineering and Science (IJRES)
ISSN (Online): 2320-9364, ISSN (Print): 2320-9356
www.ijres.org Volume 14 Issue 4 ǁ April 2026 ǁ PP. 08-13

Preparation of MoS_2@FeS_2 heterostructure and its electrocatalytic water-splitting performance

zibo Zhu[1]
[*1] *School of Materials and Chemistry, University of Shanghai for Science and Technology, Shanghai 200093, P. R. China.*
Corresponding Author: Zibo Zhu

Abstract
Electrochemical water splitting is widely recognized as a promising strategy for sustainable hydrogen production, but its practical application is still restricted by the sluggish kinetics of the hydrogen evolution reaction (HER) and especially the oxygen evolution reaction (OER). Therefore, the development of low-cost, earth-abundant, and highly efficient bifunctional electrocatalysts is of great significance for overall water splitting. In this work, a core-shell MoS_2@FeS_2 heterostructure catalyst was successfully constructed from a $FeMoO_4$ precursor through a two-step hydrothermal method. Structural characterizations confirmed the successful formation of the heterostructure with a closely contacted interface between MoS_2 and FeS_2, which provided a favorable basis for interfacial electronic coupling and synergistic catalytic effects. Electrochemical measurements demonstrated that the as-prepared MoS_2@FeS_2 catalyst exhibited excellent bifunctional electrocatalytic performance in alkaline media. For HER, the catalyst required an overpotential of only 151 mV to achieve a current density of 10 mA cm^{-2}, which was much lower than those of $FeMoO_4$, FeS_2, and MoS_2. For OER, it delivered a current density of 10 mA cm^{-2} at an overpotential of 206.8 mV and also showed a low Tafel slope
Keywords: *electrocatalysis; heterostructure; hydrogen evolution reaction; oxygen evolution reaction*

Date of Submission: 20-03-2026 Date of Acceptance: 03-04-2026

I. INTRODUCTION

Electrochemical water splitting is widely regarded as a highly promising route for sustainable hydrogen production, but its practical application is still hindered by the sluggish kinetics of the hydrogen evolution reaction (HER), and especially the oxygen evolution reaction (OER). Therefore, the development of low-cost, earth-abundant, and durable bifunctional electrocatalysts capable of efficiently driving both half-reactions is of great significance for simplifying device architecture and reducing the overall energy consumption of water electrolysis[1, 2]. Recent studies have shown that rational catalyst design strategies, including defect engineering, heteroatom doping, and heterostructure construction, are highly effective in optimizing the adsorption of reaction intermediates, accelerating charge transfer, and improving catalytic stability.

Developing synthetic routes for electrocatalysts with tunable morphology and composition to maximize the number of exposed active sites remains a challenging task [3]. Among various transition-metal-based electrocatalytic materials, metal molybdates have been widely investigated for water-splitting catalysis because of their tunable composition, abundant synergistic interactions between metal sites and Mo sites, diverse structural types, and relatively good chemical stability, particularly showing great potential in OER and bifunctional catalytic systems. For example, in materials such as $NiMoO_4$, $CoMoO_4$, and $FeMoO_4$, the synergistic effect between the transition metal and Mo can regulate the local electronic structure and influence the adsorption behavior of key reaction intermediates[4]. Meanwhile, molybdates also suffer from obvious limitations: their intrinsic electrical conductivity is usually insufficient, the exposure of active sites is limited, and in HER they often cannot simultaneously balance water dissociation and H adsorption/desorption kinetics. Therefore, single-component molybdate materials generally struggle to achieve highly efficient and simultaneous catalysis for both HER and OER. Recent studies have revealed that metal molybdates can serve as promising precursors for the rational design of transition-metal disulfide heterointerfaces through simultaneous sulfurization of both the molybdenum species and a second transition metal. Sim et al [5]. prepared a MoS_2-Ni_xS_6/NF catalyst by sulfurizing $NiMoO_4$ grown on nickel foam. After activation, MoS_2-Ni_xS_6/NF exhibited excellent HER and OER catalytic performance, requiring overpotentials of only 136 mV and 215 mV, respectively, to reach a current density of 10 mA cm^{-2}. Yang et al [6]. constructed different metal molybdates and then converted them into (NiCoFe)S_2-MoS_2 heterostructure catalysts through sulfurization. The OER overpotential of (NiCoFe-2)MoO_4 was 264 mV at 10 mA cm^{-2}, while its sulfurized derivative showed an HER overpotential of 133 mV.

Inspired by this concept, we first synthesized $FeMoO_4$ via a hydrothermal method and then used it as an Fe/Mo precursor, with thiourea as the sulfur source, to prepare a MoS_2@FeS_2 heterostructure. This precursor-derived strategy is expected to integrate the HER-favorable characteristics of MoS_2 with the iron-based sulfide component and strong interfacial synergistic effects, thereby enabling efficient bifunctional electrocatalysis for overall water splitting.

II. RESULT AND DISCUSSION

The results obtained are as discussed below

XRD was employed to analyze the crystal structure and phase composition of the $FeMoO_4$ precursor and its sulfurized product, MoS_2@FeS_2. As shown in Figure 1a, all diffraction peaks of the $FeMoO_4$ sample are in good agreement with the standard card PDF#89-2367, indicating that the as-prepared precursor possesses good crystallinity and high phase purity, thereby confirming the successful synthesis of $FeMoO_4$. After sulfurization, the XRD pattern of the sample is presented in Figure 1b. The characteristic diffraction peaks located at 9.4° and 35.5° can be assigned to the (002) and (102) crystal planes of MoS_2 (PDF#37-1492), respectively, indicating the successful formation of MoS_2 during the sulfurization process [7]. In addition, the diffraction peaks at 28.6°, 33.1°, 37.1°, 40.9°, 47.5°, 56.4°, 59.1°, 61.8°, and 64.3° can be indexed to the (111), (200), (210), (211), (220), (311), (222), (023), and (321) crystal planes of FeS_2 (PDF#42-1340), respectively, further confirming the formation of FeS_2. Notably, no obvious characteristic peaks of $FeMoO_4$ were detected after sulfurization, indicating that the $FeMoO_4$ precursor was fully sulfurized and successfully converted into the MoS_2@FeS_2 heterostructure[8].

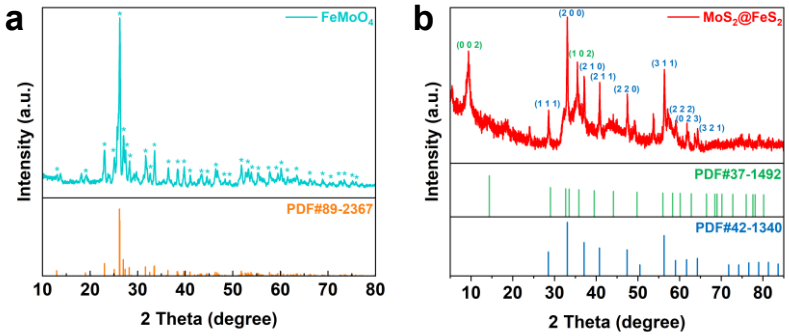

Figure1. XRD patterns of (a) $FeMoO_4$ and (b) MoS_2@FeS_2.

SEM was employed to characterize the microstructures of $FeMoO_4$, MoS_2, and MoS_2@FeS_2. As shown in Figures 2a–b, $FeMoO_4$ exhibits a distinct three-dimensional nanorod-like structure with a relatively smooth surface, which is generally consistent with the nanorod morphology of $FeMoO_4$ reported in the literature. Figures 2c–d present the SEM images of MoS_2, from which it can be seen that MoS_2 displays a relatively regular flower-like microspherical morphology assembled from a large number of curled and overlapped nanosheets, giving rise to a rough surface and a highly open structure. This type of nanosphere structure composed of ultrathin nanosheets is favorable for the formation of dislocations, grain boundaries, and defects, while the close contact among the nanospheres can promote electrical contact, thereby ensuring relatively stable electrocatalytic performance. Compared with $FeMoO_4$ and MoS_2, MoS_2@FeS_2 in Figures 2e–f exhibits a relatively loose cluster-like structure, whose surface is composed of numerous wrinkled, curled, and intertwined nanosheets, resulting in a significantly increased surface roughness. This indicates that during the sulfurization process, the original rod-like framework of $FeMoO_4$ underwent substantial reconstruction, and layered sulfide shell layers or an outer network structure were formed in situ on its surface. On the one hand, this unique morphology is beneficial for exposing more edge sites and interfacial active sites; on the other hand, it can also buffer volume variation to a certain extent and shorten ion diffusion pathways, thereby providing structural advantages for enhanced electrocatalytic performance.

In addition, the surface elemental distribution of the MoS_2@FeS_2 electrocatalyst was analyzed by energy-dispersive X-ray spectroscopy. The elemental mapping results in Figures 2g–l show that Fe, Mo, and S are all present in the sample. The color distribution in the elemental maps is somewhat non-uniform, which may be attributed to the fact that part of the FeS_2 is covered by the outer MoS_2 layer and located deeper inside the sample, leading to relatively weaker signals. In summary, combined with the SEM and elemental mapping results, it can be concluded that the present work successfully achieved the morphological transformation from rod-like $FeMoO_4$ precursors to a rough and porous MoS_2@FeS_2 heterostructure. The obtained product possesses both high surface openness and abundant heterointerfaces, thus laying a solid structural foundation for the subsequent improvement in electrocatalytic performance.

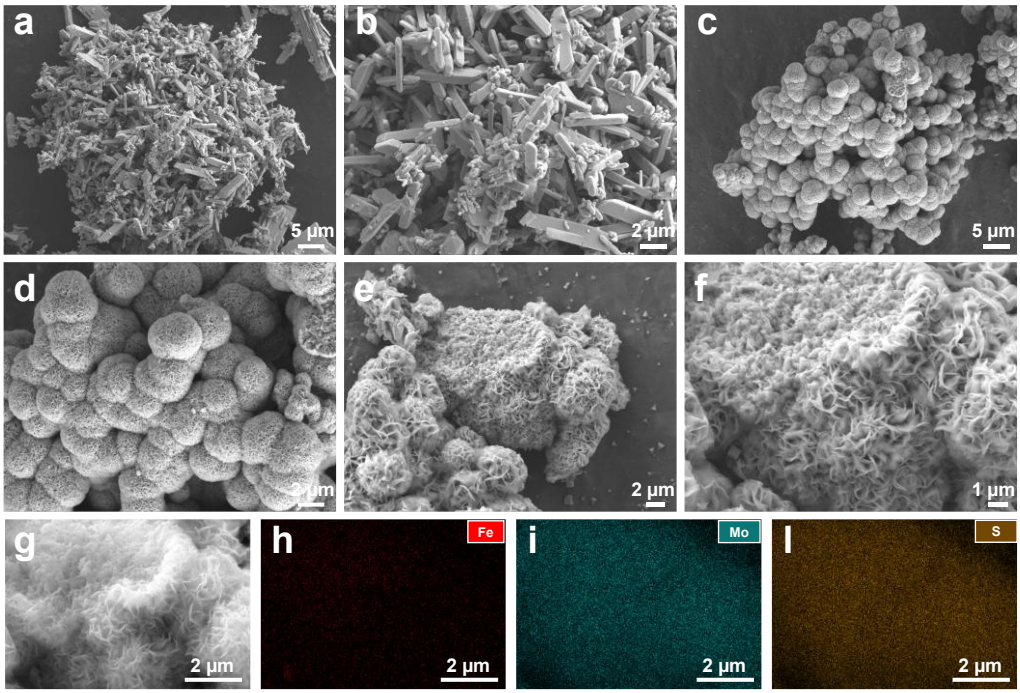

Figure2. SEM images of $FeMoO_4$; (c, d) SEM images of MoS_2; (e, f) SEM images of MoS_2@FeS_2; (g–l) MoS_2@FeS_2 and the corresponding EDS elemental mapping images.

To systematically analyze the elemental composition, chemical structure, and valence states of the MoS_2@FeS_2 composite, X-ray photoelectron spectroscopy (XPS) was performed. The high-resolution XPS spectra of Fe, Mo, S, and O in the $FeMoO_4$ and MoS_2@FeS_2 catalysts are presented in the figure. All binding energies were calibrated with reference to the C 1s peak at 284.8 eV. As shown in Figure 3a, the high-resolution Fe 2p spectrum of $FeMoO_4$ exhibits two prominent main peaks at 711.6 eV and 725.4 eV, which can be assigned to the Fe $2p_{3/2}$ and Fe $2p_{1/2}$ orbitals of Fe^{2+}, respectively, consistent with the reported valence state of Fe in $FeMoO_4$. After sulfurization, the characteristic Fe 2p peaks in MoS_2@FeS_2 are located at 711.9 eV and 725.6 eV [9]. Compared with those of the original $FeMoO_4$, these peaks show a slight positive shift but are still attributable to Fe^{2+}, indicating that the valence state of Fe remains essentially unchanged during sulfurization, while only the local electronic environment is altered. Such a slight shift is generally attributed to changes in the surrounding coordination atoms and reconstruction of the electronic structure. As shown in Figure 3b, in $FeMoO_4$, the pair of peaks at 233.1 eV and 236.2 eV correspond to the Mo $3d_{5/2}$ and Mo $3d_{3/2}$ orbitals of Mo^{6+}, respectively. The clear spin–orbit splitting confirms that Mo mainly exists in the hexavalent state in $FeMoO_4$. For the MoS_2@FeS_2 composite, a pair of strong peaks is observed at 228.6 eV and 231.8 eV, which are assigned to the Mo $3d_{5/2}$ and Mo $3d_{3/2}$ orbitals of Mo^{4+} in 1T-MoS_2, indicating the successful formation of metallic 1T-phase MoS_2 in the material. In addition, the weak peaks at 229.8 eV and 232.8 eV can be attributed to the 2H-MoS_2 phase, suggesting the presence of a small amount of the thermodynamically stable 2H phase in the sample. The peak located at 234.9 eV corresponds to Mo^{6+} species, indicating that some Mo^{4+} was slightly oxidized in air, which is a common phenomenon in MoS_2 materials. Notably, compared with pure MoS_2, the characteristic peaks of Mo^{4+} in the composite shift by about 1.4 eV toward lower binding energy, indicating significant electronic interaction (electron-transfer effect) between FeS_2 and MoS_2, thereby altering the electron cloud density around Fe and Mo.

In Figure 3c, the S 2p spectrum of MoS_2@FeS_2 shows a pair of characteristic peaks at 161.3 eV and 162.5 eV, corresponding to S $2p_{3/2}$ and S $2p_{1/2}$, respectively. Compared with pure MoS_2, these peaks shift toward lower binding energy, further confirming the interfacial electronic coupling effect between FeS_2 and MoS_2. Such electron transfer is beneficial for regulating the electronic structure of the catalyst surface, thereby enhancing its catalytic performance. Figure 3d shows the high-resolution O 1s spectrum, in which the peaks at 530.9 eV and 532.9 eV are assigned to lattice oxygen and surface chemisorbed oxygen, respectively. These results not only indicate the existence of the $FeMoO_4$ precursor-related structure, but also suggest that certain oxide characteristics are retained during the composite formation process. Meanwhile, the presence of surface-adsorbed oxygen may help provide additional active sites. In summary, the XPS results clearly demonstrate that the MoS_2@FeS_2 composite has been successfully constructed and that significant electronic interaction exists at the interface. This electronic coupling effect can effectively regulate the electronic structure of the catalyst, providing an important basis for its excellent electrocatalytic performance.

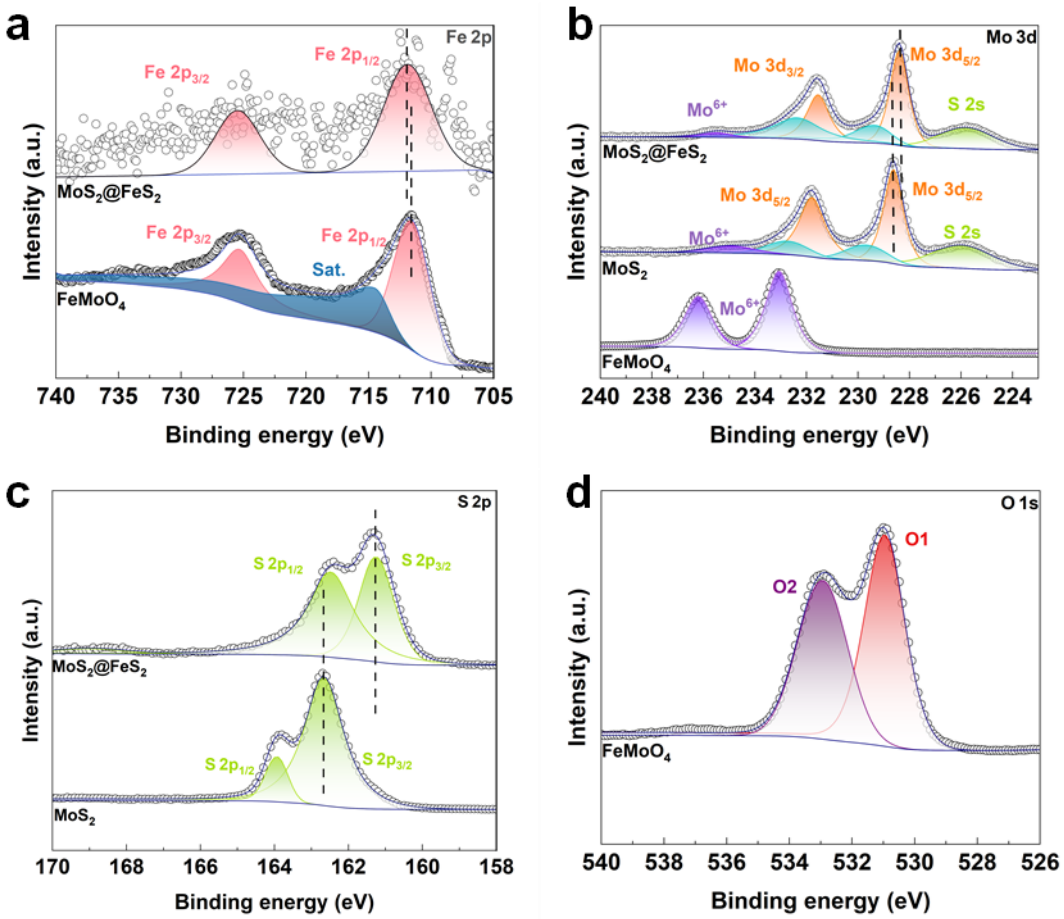

Figure3. High-resolution XPS spectra of (a) Fe, (b) Mo, (c) S, and (d) O in FeS_2@MoS_2 and $FeMoO_4$.

In a three-electrode system, we evaluated the HER catalytic activities of MoS_2@FeS_2, $FeMoO_4$, FeS_2, MoS_2, and Pt/C in 1 M KOH solution. As shown in Figure 4a, the LSV polarization curves of the catalysts were obtained using linear sweep voltammetry with 90% iR compensation. Compared with $FeMoO_4$, FeS_2, and MoS_2, MoS_2@FeS_2 exhibited the best electrocatalytic activity toward HER. Specifically, FeS_2@MoS_2 required an overpotential of only 151 mV to deliver a current density of 10 mA cm^{-2} in 1 M KOH aqueous solution, which is superior to those of conventional $FeMoO_4$ (307 mV), FeS_2 (362 mV), and MoS_2 (601 mV). The corresponding Tafel slope values were obtained by linear fitting of the LSV polarization curves in Figure 3.5a, and the results are shown in Figure 4b. According to Equation (1–3), the Volmer reaction is the rate-determining step of HER in alkaline media. Compared with $FeMoO_4$, FeS_2, and MoS_2, MoS_2@FeS_2 exhibited the smallest Tafel slope, indicating that this heterostructured catalyst undergoes a more favorable Volmer reaction under alkaline conditions and thus drives HER at a lower overpotential. In addition, electrochemical impedance spectroscopy (EIS) was used to investigate the charge-transfer behavior of the electrocatalysts. Figure 4d shows the Nyquist plots measured at −0.1 V. The EIS results reveal that the charge-transfer resistance (Rct) of FeS_2@MoS_2 is smaller than those of $FeMoO_4$, FeS_2, and MoS_2, indicating a higher charge-transfer efficiency for MoS_2@FeS_2. In summary, MoS_2@FeS_2 exhibits excellent electrocatalytic activity toward HER, with low overpotential, a small Tafel slope, and low charge-transfer resistance.

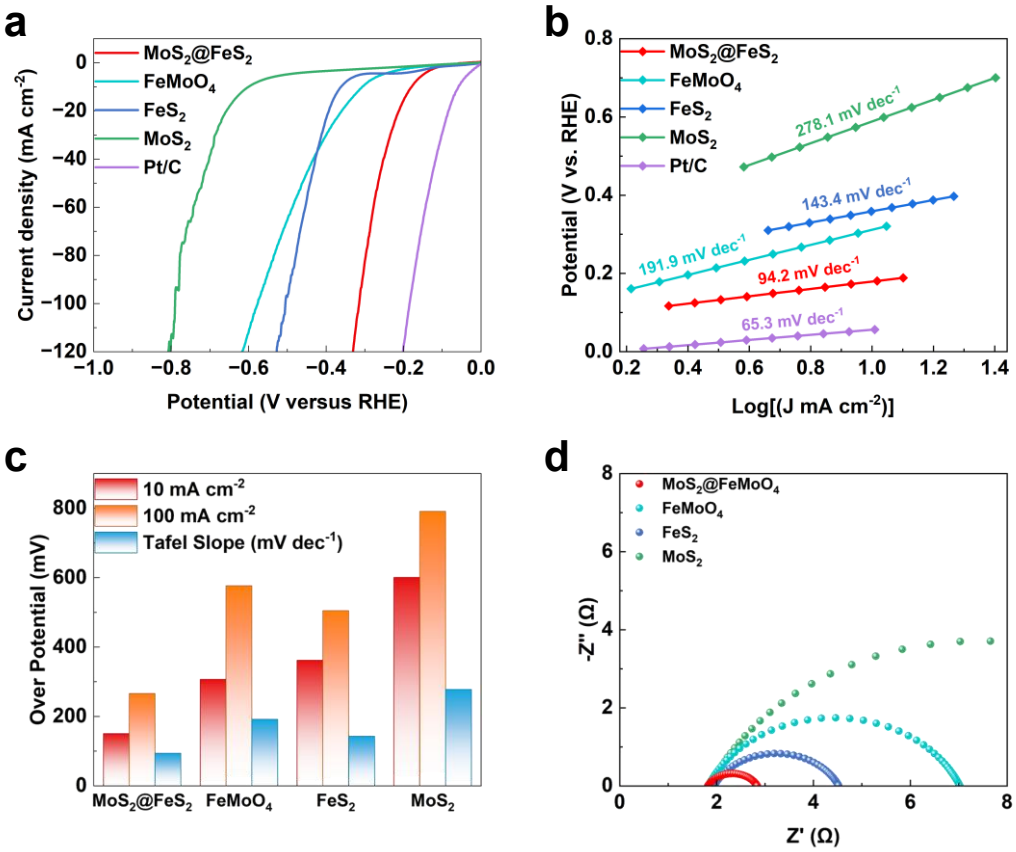

Figure4. Electrochemical performance measurements: (a) LSV curves; (b) Tafel slopes; (c) comparison of overpotentials at different current densities and Tafel slopes; (d) EIS curves.

In a typical three-electrode system, the OER performance of the as-prepared MoS_2@FeS_2 in alkaline electrolyte was also evaluated. For comparison, the OER activities of $FeMoO_4$, FeS_2, MoS_2, and RuO_2 were measured under the same conditions. The catalytic activities of the samples were assessed in 1 M KOH. According to the cyclic voltammetry results (scan rate: 5 mV s^{-1}), the MoS_2@FeS_2 composite electrocatalyst required an overpotential of only 206.8 mV to achieve a current density of 10 mA cm^{-2}, exhibiting significantly superior catalytic performance compared with the reference samples. As shown in Figure 4a, under the same testing conditions, $FeMoO_4$ and $FeMoO_4$ required overpotentials of 268 mV and 322 mV, respectively, to reach the same current density, whereas pure MoS_2 showed no OER activity in 1 M KOH and was therefore excluded from comparison. These results indicate that the combination of MoS_2 and FeS_2 effectively enhances the electrocatalytic activity of the material.

When the current density was increased to 100 mA cm^{-2}, the overpotentials of MoS_2@FeS_2, $FeMoO_4$, and FeS_2 were 291.8, 371.8, and 404.8 mV, respectively, further demonstrating the high electrochemical OER activity of MoS_2@FeS_2 in alkaline electrolyte. The Tafel slope is an important parameter for evaluating the kinetic behavior of catalysts during the OER process and is usually derived from the linear region of the Tafel plot at low current densities. As shown in Figure 4b, MoS_2@FeS_2 exhibits a Tafel slope of 71.2 mV dec^{-1}, which is much lower than those of $FeMoO_4$ (90.3 mV dec^{-1}) and FeS_2 (109.7 mV dec^{-1}), indicating that the MoS_2@FeS_2 heterostructure possesses faster reaction kinetics. It is well known that the strong coupling generated at heterostructure interfaces can accelerate the catalytic reaction process. Electrochemical impedance spectroscopy was further employed to investigate the charge-transfer kinetics of MoS_2@FeS_2 during the OER process. As shown in Figure 4d, MoS_2@FeS_2 exhibits the smallest semicircle diameter in the medium- to high-frequency region, indicating a lower charge-transfer resistance and faster charge-transfer kinetics.

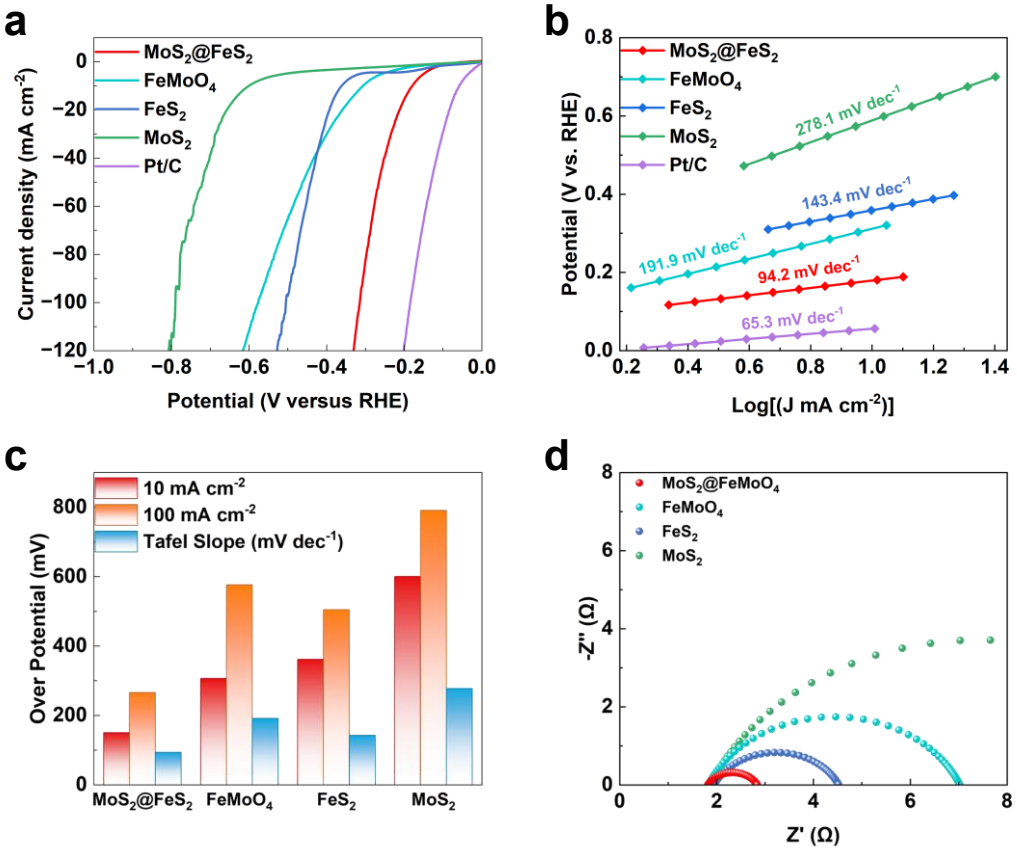

Figure5. Electrochemical performance measurements: (a) LSV curves; (b) Tafel slopes; (c) comparison of overpotentials at different current densities and Tafel slopes; (d) EIS curves.

III. CONCLUSION

In summary, this chapter successfully constructed a core–shell MoS_2@FeS_2 heterostructure catalyst using $FeMoO_4$ as the precursor via a two-step hydrothermal method. The results indicate that the obtained sample retains well-defined heterostructural characteristics, and a closely contacted interface is formed between the MoS_2 and FeS_2 phases, thereby providing a structural basis for subsequent interfacial electronic coupling and catalytic synergistic effects. Electrochemical tests demonstrate that the MoS_2@FeS_2 heterostructure exhibits excellent catalytic activity for both HER and OER**.** For HER, the catalyst shows a low hydrogen evolution overpotential and fast reaction kinetics; for OER, it also exhibits a low overpotential and favorable oxygen evolution reaction rate, indicating that the construction of the MoS_2@FeS_2 heterointerface can effectively enhance bifunctional catalytic performance. In addition, MoS_2@FeS_2 can operate stably for 100 h during both HER and OER tests at a current density of 10 mA cm^{-2}, demonstrating its excellent electrochemical stability. Therefore, the excellent bifunctional catalytic performance of MoS_2@FeS_2 can be attributed to the electronic structure modulation induced by the heterointerface, the synergistic effect of active sites, and the optimized adsorption behavior of reaction intermediates.

REFERENCES

[1]. Yang, D.; Zhang, C.; Qin, Y.; Yue, Y.; Liu, Y.; Shi, X.; Hua, K.; An, X.; Jin, L.; Zhang, Y.; et al. Nat. Commun. 2025, 16 1, 7236.
[2]. Wu, B.; Su, W.; Zhu, P.; Xu, J.; Yuan, K.; Li, L.; Chen, Y. Adv. Mater 2025, 37 40, e07842.
[3]. Shi, W.; Shen, T.; Xing, C.; Sun, K.; Yan, Q.; Niu, W.; Yang, X.; Li, J.; Wei, C.; Wang, R.; et al. Science 2025, 387 6735, 791-796.
[4]. Townsend, W. J. V.; López-Alcalá, D.; Bird, M. A.; Jordan, J. W.; Rance, G. A.; Biskupek, J.; Kaiser, U.; Baldoví, J. J.; Walsh, D. A.; Johnson, L. R.; et al. Nat. Commun. 2025, 16 1, 4460.
[5]. Li, C.; Ye, B.; Ouyang, B.; Zhang, T.; Tang, T.; Qiu, Z.; Li, S.; Li, Y.; Chen, R.; Wen, W.; et al. Adv. Mater 2025, 37 28, 2501381.
[6]. Zuo, S.; Wu, Z.-P.; Xu, D.; Ahmad, R.; Zheng, L.; Zhang, J.; Zhao, L.; Huang, W.; Al Qahtani, H.; Han, Y.; et al. Nat. Commun. 2024, 15 1, 9514.
[7]. Li, Y.; Zhao, J.; Zhang, S.; Fan, Y.; Kuo, C.-Y.; Ku, Y.-C.; Chan, T.-S.; Kao, C.-W.; Huang, Y.-C.; Chen, C.-T.; et al. J.Am. Chem. Soc 2025, 147 30, 26854-26864.
[8]. She, S.; Chen, C.; Fan, K.; Chen, G.; Zhu, Y.; Guan, D.; Huang, Y.-C.; Chen, H.-C.; Lin, Z.; Wong, H. F.; et al. J.Am. Chem. Soc 2025, 147 28, 24392-24402.
[9]. Xu, F.; Yang, Q.; Xu, Z.; Le, H.; Zhou, T.; Wang, Y.; Mu, S. Nano Energy 2025, 142, 111254.